First-principles studies of spin-phonon coupling in monolayer $Cr_2Ge_2Te_6$

B. H. Zhang,[1] Y. S. Hou,[2] Z. Wang,[1] and R. Q. Wu[2,*]

[1]*State Key Laboratory of Surface Physics, Key Laboratory of Computational Physical Sciences, and Department of Physics, Fudan University, Shanghai 200433, China*

[2]*Department of Physics and Astronomy, University of California, Irvine, California 92697, USA*

(Received 27 September 2019; revised manuscript received 12 December 2019; published 30 December 2019)

We perform systematic first-principles calculations to investigate the spin-phonon coupling (SPC) of $Cr_2Ge_2Te_6$ (CGT) monolayer (ML). It is found that the E_g phonon mode at 211.8 cm^{-1} may have a SPC as large as 3.19 cm^{-1}, as it alters the direct exchange interaction across Cr-Cr pairs. The strength of SPC of the CGT ML can be decreased by an in-plane lattice stretch. These results provide useful insights for the understanding of SPC in two-dimensional magnetic semiconductors and may guide the design of spintronic and spin Seebeck materials and devices.

DOI: 10.1103/PhysRevB.100.224427

I. INTRODUCTION

Two-dimensional (2D) van der Waals (vdW) monolayers (MLs) have attracted considerable research interest in the last decade because of their unique physical property, adaptability, and high integrability with other materials for the design of novel electronic and spintronic devices [1–6]. One of the challenges is to generate stable magnetization in these materials at a reasonably high temperature so that they can be used to filter spin currents or to magnetize topological surface states, to name a few possibilities [7,8]. While magnetism can be induced in many nonmagnetic 2D materials such as graphene, hex-BN, and MoS_2 by introducing dopants, defects, and edges [9,10], several new ferromagnetic (FM) vdW monolayers such as recently synthesized $Cr_2Ge_2Te_6$ (CGT) [1] and CrI_3 [11] appear to be more attractive for fundamental studies as well as for applications [12], which have inspired a new wave of research interest in exploring and manipulating 2D magnetic materials [13,14]. Due to the presence of sizable magnetic anisotropy energy, the FM ordering of these monolayers may sustain at finite temperature, unlike what was predicted by the Mermin-Wigner theorem in the isotropic Heisenberg model [9]. Many experiments later have demonstrated that CGT and related 2D vdW magnetic MLs have many other remarkable merits [1,15–17], such as a large Kerr rotation angle, a giant modulation of the channel resistance, and a high thermoelectric performance. Integrating CGT with a topological insulator Bi_2Te_3 was found to greatly improve the electrical transport properties and enlarge the anomalous Hall conductivity [18].

To control and utilize the ferromagnetism of CGT and other 2D vdW magnetic MLs, a comprehensive study of their spin-phonon coupling (SPC) is crucial, because SPC plays an important role in magnetic fluctuation, magnonic dissipation, as well as in establishing the long-range FM order in these materials [3,19–28]. As far as we know, no quantitative theoretical study has been done for the SPC in 2D magnetic MLs, and only a handful of experimental measurements of the SPC in CGT ML (e.g., using high-resolution micro-Raman scattering [3,20,24,25,27] and inelastic neutron scattering [21]) have been attempted [2]. This calls for more systematic and quantitative investigations for SPC in these new systems, so as to establish rules for guiding the 2D magnetic materials design.

In this work, we used the first-principles calculations to systematically investigate the SPC in the CGT ML. Our results show that the SPC of the CGT ML varies with different vibrational modes. Especially, the E_g mode at 211.8 cm^{-1} shows the largest SPC, up to 3.19 cm^{-1}, which can be understood as a result of the strong interplay between the Cr-Cr direct exchange interaction and the lattice deformation. Furthermore, we demonstrated that the SPC can be significantly enhanced by an in-plane compressive strain. Our work thus provides a deep insight regarding the SPC in 2D vdW magnetic monolayers and should be useful for their exploitation in various devices.

II. METHODS

The CGT ML is a 2D FM semiconductor, and can be mechanically exfoliated from the bulk CGT [29]. Figures 1(a) and 1(b) show the crystal structure of the CGT ML. There are two Cr, two Ge, and six Te atoms in the unit cell (u.c.). The magnetic Cr ions form a honeycomb lattice and locate at the center of a slightly distorted octahedron formed by six Te atoms. Our first-principles calculations were performed using the projector-augmented wave method as implemented in the Vienna *Ab initio* Simulation Package (VASP). The exchange-correlation interactions were described by the generalized-gradient approximation (GGA) with the Perdew-Burke-Ernzerhof (PBE) functional [30]. The strong correction effect among the 3*d* electrons of Cr was described by adding an onsite Coulomb and exchange parameters $U = 1.5$ eV and $J = 0.5$ eV, respectively [1,15,31]. An energy cutoff of 450 eV was used for the plane-wave basis expansion. All atomic positions were fully relaxed until the force acting on each atom became smaller than 1×10^{-5} eV/Å. We used the experimental lattice constant in the lateral plane for the CGT

*wur@uci.edu

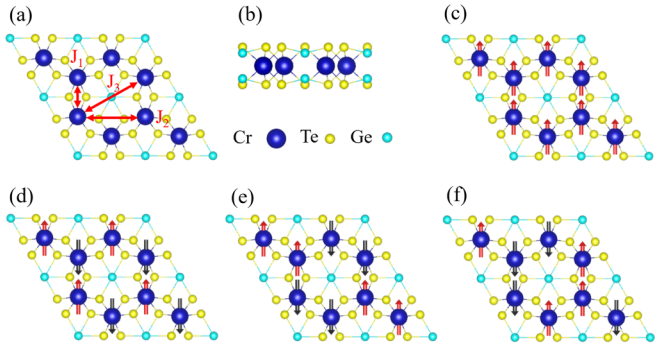

FIG. 1. (a) Top view and (b) side view of ML CGT. The considered exchange paths are shown by the red double arrows in (a). The possible magnetic configurations of ML CGT are (c) FM, (d) Néel-AFM, (e) stripy-AFM, and (f) zigzag-AFM orders.

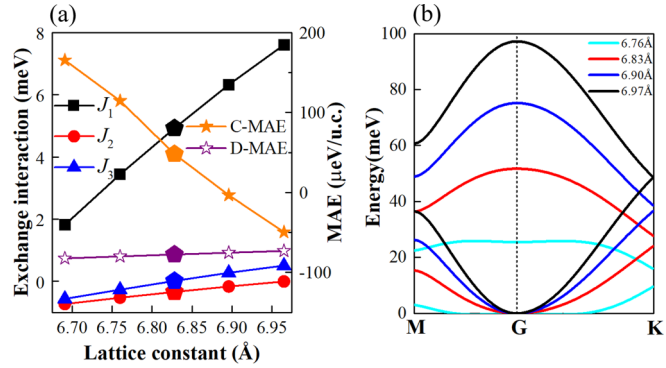

FIG. 2. The dependences of (a) the magnetic-exchange interactions, magnetic anisotropy energies, and (b) spin waves on the lattice constant. The pentagonal symbols in (a) and the red lines in (b) give the magnetic anisotropy energy and the spin wave of ML CGT with the experimental lattice constant.

ML, $a = b = 6.83$ Å, and adopted a slab model with a vacuum space of 17 Å to avoid the interaction between periodic images. The Brillouin zone was sampled with a $12 \times 12 \times 1$ k-point mesh in the primitive cell. A $6 \times 6 \times 1$ mesh was used for the $2 \times 2 \times 1$ supercell. In calculating the phonon spectrum, we used a $4 \times 4 \times 1$ supercell and a $3 \times 3 \times 1$ k-point mesh.

III. RESULTS

A. Magnetic properties of 2D ML CGT

We first determine the magnetic ground state of the CGT ML, using the experimental lattice constant. The total energy of the FM state (−47.155 eV/u.c.) is sizably lower than those of three other magnetic states, namely the Néel antiferromagnetic (AFM) (Néel-AFM, −47.090 eV/u.c.), stripy AFM (stripy-AFM, −47.118 eV/u.c.), and zigzag AFM (zigzag-AFM, −47.140 eV/u.c.) [Figs. 1(c)–1(f)]. This clearly shows that the FM order is the ground state of the CGT ML, consistent with experimental observations [32].

Our calculations of the magnetic anisotropy energy (MAE) show that the CGT ML with the experimental lattice constant has an out-of-plane easy axis. The magnetic anisotropy energy of CGT ML is composed of magnetocrystalline anisotropy energy (C-MAE) and magnetic dipolar anisotropy energy (D-MAE). As depicted in Fig. 2(a), D-MAE is always negative (prefers an in-plane magnetization), whereas C-MAE turns from positive to negative as the lattice constant increases. As a result, the magnetic easy axis is out of plane when a compressive strain of >0.41% is applied. Since C-MAE strongly depends on the lattice constant, it is feasible to enhance the out-of-plane magnetic anisotropy of the CGT ML through a compressive strain, other than using heterostructures or absorbates as proposed in the literature [33,34].

To investigate the spin excitations, we determine the exchange interactions between the magnetic ions Cr, utilizing a spin Hamiltonian as

$$H = -J_1 \sum_{\langle ij \rangle} \vec{S}_i \cdot \vec{S}_j - J_2 \sum_{\langle\langle ij \rangle\rangle} \vec{S}_i \cdot \vec{S}_j - J_3 \sum_{\langle\langle\langle ij \rangle\rangle\rangle} \vec{S}_i \cdot \vec{S}_j. \quad (1)$$

Here, J_1, J_2, and J_3 are the exchange interactions between the nearest neighbors, second-nearest neighbors, and third-nearest neighbors [Fig. 1(a)]. Note that positive values of $J_i (i = 1, 2, 3)$ mean FM interactions and negative ones mean AFM interactions. Based on Eq. (1), the energies of different spin orders shown in Figs. 1(c)–1(f) are given as follows:

$$E_{\text{FM/Néel}} = E_0 \mp 12J_1|\vec{S}|^2 - 24J_2|\vec{S}|^2 \mp 12J_3|\vec{S}|^2, \quad (2)$$

$$E_{\text{stripy/zigzag}} = E_0 \pm 4J_1|\vec{S}|^2 + 8J_2|\vec{S}|^2 \mp 12J_3|\vec{S}|^2. \quad (3)$$

In Eqs. (2) and (3), spin S for each Cr atom is 3/2. Our calculations show that $J_1 = 4.92$ meV, $J_2 = -0.31$ meV, and $J_3 = 0.01$ meV, which agrees well with previous studies [15,35]. The large FM J_1 results from the competition between the direct exchange between Cr–Cr sites and the superexchange mediated through the Te ions, and strongly depends on the Cr-Cr distance. It is conceivable that J_1 changes when the CGT lattice is either stretched or compressed. This is confirmed in Fig. 2(a), which shows that J_1, J_2, and J_3 increase rapidly with lattice expansion in a range from 6.69 to 6.97 Å. Especially, the slope of the black curve in Fig. 2(a) indicates that the coefficient of the variation of J_1 with lattice expansion is as large as 21.13 meV/Å. As J_1 results from the competition between the negative Cr-Cr direct exchange and positive Cr-Te-Cr superexchange, this trend indicates the rapid decrease of Cr-Cr direct-exchange interaction as the lattice expands. For this reason, the FM state becomes more stable due to superexchange interactions when the lattice is stretched.

To study the spin-wave spectrum of the CGT ML, we recast Eq. (1) in terms of the spin ladder operators $\hat{S}^{\pm} = \hat{S}^x \pm i\hat{S}^y$ and $\hat{S}^z$. For the low-energy excitations, we obtain the spin-wave spectrum as Eq. (4), by introducing the Holstein-Primakoff transformation [36] and Fourier transform (details are given in Part I in the Supplemental Material [37]).

$$\hbar\omega = 2S \sum_{n=1}^{3} Z_n J_n \pm 2S \left| \sum_{n=1}^{3} J_n \sum_{\delta_n} e^{i\vec{k}\cdot\vec{\delta}_n} \right|. \quad (4)$$

Here, $Z_1 = 3$, $Z_2 = 6$, and $Z_3 = 3$ are the first, second, and third coordination numbers. The acoustic and optical modes of spin waves are obtained when the plus and minus sign are taken, respectively. As shown in Fig. 2(b), the energy of spin

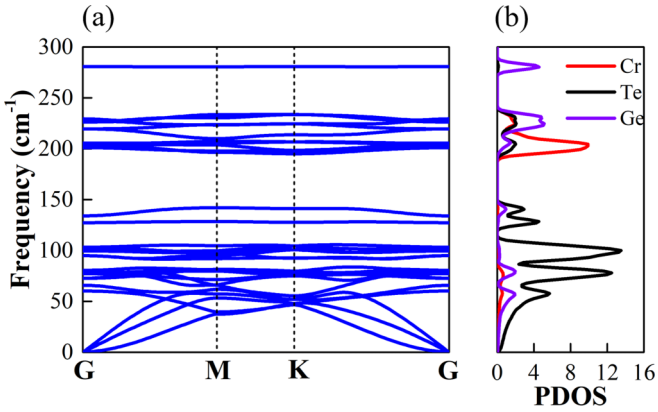

FIG. 3. (a) Phonon spectrum and (b) PDOSs of the CGT ML. The red, black, and violet lines correspond to the PDOSs of Cr, Te, and Ge, respectively.

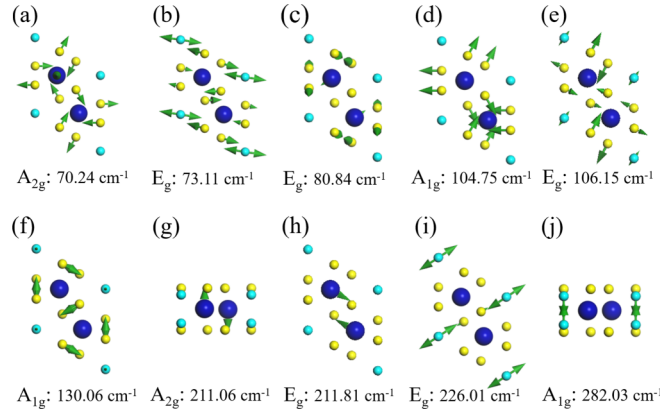

FIG. 4. Schematic representations of the eigenvectors for all Raman-active distinct phonon vibrational modes at the Γ point. Cr, Ge, and Te atoms are represented by the blue, cyan, and yellow balls. The arrows show the directions and amplitudes of the atomic displacements in each mode.

waves increases as the lattice constant increases. Note that the spin waves with a lattice constant $a = 6.69$ Å are not included in Fig. 2(b) since the CGT ML becomes zigzag-AFM state in this case (The FM→AFM phase transition occurs when the lattice constant is less than 6.75 Å as shown in Part II in the Supplemental Material) [37]. Again, the stiffness of spin waves and magnetic ground state of the CGT ML can be tuned by applying a strain, and a strong spin-phonon coupling is hence expected [35].

B. Phonon properties of 2D ML CGT

The calculated phonon band dispersion of the 2D CGT ML is shown in Fig. 3(a). There is no negative phonon branch, indicating that this system is dynamically stable. Furthermore, 2D CGT ML is thermally stable, as demonstrated by the *ab initio* dynamics simulations (see Part III in the Supplemental Material) [37]. A remarkable feature of the phonon dispersion is the abundance of flat bands, which can also be appreciated from the numerous sharp peaks in curves of the phonon density of states (PDOS) as shown in Fig. 3(b). The PDOSs of the low-frequency modes ($<150\,\mathrm{cm}^{-1}$) are mainly dominated by motions of Te atoms due to their larger mass, whereas the mid-frequency modes ($180 \sim 240\,\mathrm{cm}^{-1}$) mainly result from motions of Cr atoms. The high-frequency modes ($> 260\,\mathrm{cm}^{-1}$) mainly involve motions of Ge atoms. The flat bands in Fig. 3(a) and the weak coupling between different atoms in Fig. 3(b) clearly suggest that most vibration modes are rather local. As the ratio of Cr motion is small in the low-energy acoustic modes, we focus on the optical modes around $200\,\mathrm{cm}^{-1}$ for studies of SPC because there is a large ratio of Cr motion. In Table I, we give the irreducible symmetry representations of vibration modes of the CGT ML with the point group S_6, which can be expressed as $\Gamma = A_{1u} + 3A_{2u} + 3A_{1g} + 2A_{2g} + 5E_g + 4E_u$. The infrared-active vibrational modes have the A_{1u}, $3A_{2u}$, and $4E_u$ symmetries, whereas the Raman-active modes have the $3A_{1g}$, $2A_{2g}$, and $5E_g$ symmetries.

Here we focus on the Raman-active modes since they are measured in experiments [3]. The eigenvectors of these modes with the $3A_{1g}$, $2A_{2g}$, and $5E_g$ symmetries are schematically shown in Fig. 4. For the degenerate modes, we only show one branch of them. The modes in Figs. 4(a)–4(f) mainly stem from motions of Te atoms around Cr; and those in Figs. 4(g) and 4(h) show the out-of-plane and in-plane Cr motions. In particular, the E_g mode at $211.81\,\mathrm{cm}^{-1}$ in Fig. 4(h) mainly involves antiphase motions of the two Cr atoms. Finally, the E_g and A_{1g} modes shown in Figs. 4(i) and 4(j) consist of in-plane and out-of-plane vibrations of Ge layers, respectively.

C. SPC of MLCGT

Now we investigate the SPC in the CGT ML with the frozen magnon approach proposed in Refs. [23,26]. The total

TABLE I. Frequencies of the phonon vibrational modes for CGT ML at the Γ point.

Mode	Frequency (cm^{-1})	Symmetry	Mode	Frequency (cm^{-1})	Symmetry
1	59.38	A_{2u}	15	130.06	A_{1g}
2	70.24	A_{2g}	16	140.17	A_{2u}
3,4	73.11	E_g	17,18	205.96	E_u
5,6	78.12	E_u	19	211.06	A_{2g}
7,8	80.84	E_g	20,21	211.81	E_g
9,10	97.99	E_u	22,23	226.01	E_g
11	102.65	A_{1u}	24,25	232.35	E_u
12	104.75	A_{1g}	26	238.38	A_{2u}
13,14	106.15	E_g	27	282.03	A_{1g}

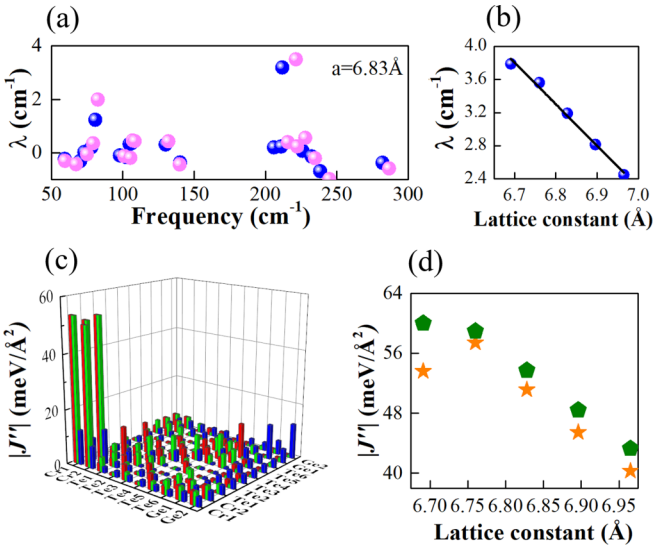

FIG. 5. (a) The dispersion of SPC of CGT in the experimental lattice constant $a = 6.83$ Å. Blue and pink balls represent results using the PBE and PBEsol functionals, respectively. (b) The dependence of the SPC parameter of the 211.81-cm^{-1} mode on lattice constant. (c) Atom-resolved diagonal $|J''| = |\partial^2 J_{ij}/\partial u_\eta \partial u_{\eta'}|$; the red, green, and blue bars represent $|J''_{xx}|$, $|J''_{yy}|$, and $|J''_{zz}|$, respectively. (d) The dependences of $|\partial^2 J_x/\partial u_{Cr1}\partial u_{Cr1}|$ (pentagons) and $|\partial^2 J_x/\partial u_{Cr1}\partial u_{Cr2}|$ (orange stars) on the lattice constant.

energy E can be expressed as

$$E = E_0 - \frac{1}{2}\sum_{ij} J_{ij}\vec{S}_i \cdot \vec{S}_j + \frac{1}{2}\sum_{\eta\eta'}\left(\tilde{C}_{\eta,\eta'} - \frac{1}{2}\sum_{ij}\frac{\partial^2 J_{ij}}{\partial u_\eta \partial u_{\eta'}}\langle \vec{S}_i \cdot \vec{S}_j\rangle\right)u_\eta u_{\eta'},$$
$$\eta \equiv \{n, \beta\}. \tag{5}$$

In Eq. (5), the first and second terms are the paramagnetic (PM) energy and the exchange-interaction energy without vibrations and the third term is the energy due to the presence of phonon, respectively. η represents the direction ($\beta = x, y, z$) of motion of the nth atom. For J_{ij}, we only consider J_1 since it plays the major role in spin dynamics and it strongly depends on the separation between adjacent Cr atoms. $\tilde{C}_{\eta,\eta'}$ is the force constant for a magnetic ordering. $\partial^2 J_{ij}/\partial u_\eta \partial u_\eta$ is the second derivative of the exchange interaction J_1 with respect to atomic displacements. The sums for i and j run over the magnetic atoms. In the CGT ML, we obtain $\tilde{C}^{\rm FM} = C - 3J''S^2$ and $\tilde{C}^{\rm AFM} = C + 3J''S^2$, where $\tilde{C}^{\rm FM}$ and $\tilde{C}^{\rm AFM}$ are the force-constant matrices obtained by the first-principles calculations in the cases of the FM and AFM states. C is the force constant for the PM phase. Therefore, the coupling parameter λ_i for each mode ψ_i can be easily calculated according to the expression

$$\lambda_i = \langle\psi_i|\frac{-3J''}{2S^2\omega_i}|\psi_i\rangle. \tag{6}$$

Here, ω_i represents the vibrational frequencies of the PM states, and ψ_i is the mass-weighted eigenvector.

Figure 5(a) shows the SPC coefficients of different modes for the CGT ML with the experimental lattice constant. For comparison, results of PBEsol functional [38] are also given (more PBEsol results are shown in Part IV in the Supplemental Material) [37]. There is no significant difference between PBE and PBEsol for the determination of SPC coefficients, so in the following we still only focus our discussion on the PBE results. Obviously, the strength of SPC depends on the involvement of Cr motion in each vibration mode. For example, the E_g mode at 211.81 cm^{-1} that has the largest Cr component in Fig. 3(b) also shows the largest SPC, about 3.19 cm^{-1}. The other sizable SPC is about 1.24 cm^{-1}, appearing in the E_g mode at 80.84 cm^{-1}, which also involves vibrations of Cr atoms. As Cr motions of the A_{2g} mode at 211.06 cm^{-1} are out of plane and less affect the Cr-Cr distance, its SPC is only about 0.24 cm^{-1}. Most of the remaining Raman-active modes have weak SPC coefficients since they mainly involve motions of either Te or Ge atoms. Importantly, the SPC coefficient of the 211.81-cm^{-1} mode also changes rapidly with the lattice strain, as shown in Fig. 5(b). Nonetheless, its dependence on the lattice constant is opposite to that of J_1, as SPC of the CGT ML enhances in the compression side.

Now let us dig deeper into the SPC with respect to the atomic motions in different vibrational modes. Both Cr-Te-Cr superexchange and Cr-Cr direct-exchange interactions are modulated by vibrations. As depicted in Fig. 5(c), $J'' = \partial^2 J_{ij}/\partial u_\eta \partial u_{\eta'}$ changes much more as we displace Cr atoms in the plane than when we move Te atoms ($|\partial^2 J_{xx,yy}/\partial u_{\rm Cr}\partial u_{\rm Cr}| \approx 54$ meV/Å^2, $|\partial^2 J/\partial u_{\rm Te}\partial u_{\rm Te}| \approx 13$ meV/Å^2). Since motions of Te only affect the superexchange interaction, we may conclude that the direct-exchange interaction across Cr pairs (J_D) plays the dominant role for the SPC. J_D varies exponentially with the change of Cr-Cr distance (Δr), i.e., $J_D(r + \Delta r) \approx J_D(r)e^{-\alpha\Delta r}$ [26,38]. Here, α is estimated to be about 5 Å^{-1} from the $3d$ orbitals of Cr^{3+} ions [38]. It is easy to show that J''_{xx} follows J_D as $J''_{xx} \approx \partial^2 J_D/\partial x^2 = (1/4)\partial^2 J_D/\partial(\Delta r)^2 \approx (1/4)\alpha^2 J_D(r)e^{-\alpha\Delta r} \approx (1/4)\alpha^2 J_D(r)$. This qualitatively explains the decrease of J_1 in Fig. 2(a), and the increase of $|J''_{xx}|$ in Fig. 5(d) when lattice is compressed. Since the SPC at 211.81 cm^{-1} is in proportion to $|J''_{xx}|$ of Cr atoms, the SPC will also be enhanced as shown in Fig. 5(b). Furthermore, if simply assuming that the decrease of J_1 arises totally from J_D, we can yield $\alpha \approx 4$ Å^{-1} by comparing the slope of $|J''_{xx}|$ and J_1, which compares well with that estimated from atomic orbitals, $\alpha \approx 5$ Å^{-1}.

IV. CONCLUSIONS

By means of the first-principles calculations, we systematically investigated the magnetic-exchange interaction, spin waves, phonons, and SPC of the 2D magnetic CGT ML. The magnetic-exchange interaction J and spin-wave stiffness quickly increase as lattice constant expands. Frozen magnon calculations indicate that the E_g phonon mode at 211.81 cm^{-1} has the largest SPC, about 3.19 cm^{-1}, because it corresponds to the largest in-plane Cr motions. We found that the Cr-Cr direct exchange is much more sensitive to this vibration than the Cr-Te-Cr superexchange interaction. This study gives useful insights for the control of magnetic and phononic properties

of 2D magnetic materials. The tunable SPC may find use in many applications such as spin filtering, spin Seebeck, and spin-wave control, to name a few.

ACKNOWLEDGMENTS

The work was supported by the US DOE-BES under Grant No. DE-FG02-05ER46237.

[1] C. Gong, L. Li, Z. Li, H. Ji, A. Stern, Y. Xia, T. Cao, W. Bao, C. Wang, Y. Wang, Z. Q. Qiu, R. J. Cava, S. G. Louie, J. Xia, and X. Zhang, Nature (London) **546**, 265 (2017).

[2] L. Webster, L. Liang, and J. A. Yan, Phys. Chem. Chem. Phys. **20**, 23546 (2018).

[3] Y. Tian, M. J. Gray, H. W. Ji, R. J. Cava, and K. S. Burch, 2D Mater. **3**, 025035 (2016).

[4] W. Choi, N. Choudhary, G. H. Han, J. Park, D. Akinwande, and Y. H. Lee, Mater. Today **20**, 116 (2017).

[5] A. Gupta, T. Sakthivel, and S. Seal, Prog. Mater Sci. **73**, 44 (2015).

[6] A. K. Geim and K. S. Novoselov, Nat. Mater. **6**, 183 (2007).

[7] Y. Hou, J. Kim, and R. Wu, Sci. Adv. **5**, eaaw1874 (2019).

[8] T. Song, X. Cai, M. W.-Y. Tu, X. Zhang, B. Huang, N. P. Wilson, K. L. Seyler, L. Zhu, T. Taniguchi, and K. Watanabe, Science **360**, 1214 (2018).

[9] O. V. Yazyev and L. Helm, Phys. Rev. B **75**, 125408 (2007).

[10] J. Cervenka, M. I. Katsnelson, and C. F. J. Flipse, Nat. Phys. **5**, 840 (2009).

[11] B. Huang, G. Clark, E. Navarro-Moratalla, D. R. Klein, R. Cheng, K. L. Seyler, D. Zhong, E. Schmidgall, M. A. McGuire, and D. H. Cobden, Nature **546**, 270 (2017).

[12] B. Shabbir, M. Nadeem, Z. Dai, M. S. Fuhrer, Q.-K. Xue, X. Wang, and Q. Bao, Appl. Phys. Rev. **5**, 041105 (2018).

[13] C. Gong and X. Zhang, Science **363**, eaav4450 (2019).

[14] K. S. Burch, D. Mandrus, and J.-G. Park, Nature (London) **563**, 47 (2018).

[15] Y. M. Fang, S. Q. Wu, Z. Z. Zhu, and G. Y. Guo, Phys. Rev. B **98**, 125416 (2018).

[16] M. Mogi, A. Tsukazaki, Y. Kaneko, R. Yoshimi, K. S. Takahashi, M. Kawasaki, and Y. Tokura, APL Mater. **6**, 091104 (2018).

[17] W. Y. Xing, Y. Y. Chen, P. M. Odenthal, X. Zhang, W. Yuan, T. Su, Q. Song, T. Y. Wang, J. N. Zhong, S. Jia, X. C. Xie, Y. Li, and W. Han, 2D Mater. **4**, 024009 (2017).

[18] L. D. Alegria, H. Ji, N. Yao, J. J. Clarke, R. J. Cava, and J. R. Petta, Appl. Phys. Lett. **105**, 053512 (2014).

[19] R. Werner, C. Gros, and M. Braden, Phys. Rev. B **59**, 14356 (1999).

[20] T. Rudolf, C. Kant, F. Mayr, J. Hemberger, V. Tsurkan, and A. Loidl, Phys. Rev. B **75**, 052410 (2007).

[21] S. Petit, F. Moussa, M. Hennion, S. Pailhes, L. Pinsard-Gaudart, and A. Ivanov, Phys. Rev. Lett. **99**, 266604 (2007).

[22] J. H. Lee and K. M. Rabe, Phys. Rev. B **84**, 104440 (2011).

[23] A. Kumar, C. J. Fennie, and K. M. Rabe, Phys. Rev. B **86**, 184429 (2012).

[24] C. Kant, J. Deisenhofer, T. Rudolf, F. Mayr, F. Schrettle, A. Loidl, V. Gnezdilov, D. Wulferding, P. Lemmens, and V. Tsurkan, Phys. Rev. B **80**, 214417 (2009).

[25] M. N. Iliev, H. Guo, and A. Gupta, Appl. Phys. Lett. **90**, 151914 (2007).

[26] C. J. Fennie and K. M. Rabe, Phys. Rev. Lett. **96**, 205505 (2006).

[27] L. D. Casto, A. J. Clune, M. O. Yokosuk, J. L. Musfeldt, T. J. Williams, H. L. Zhuang, M. W. Lin, K. Xiao, R. G. Hennig, B. C. Sales, J. Q. Yan, and D. Mandrus, APL Mater. **3**, 041515 (2015).

[28] E. Aytan, B. Debnath, F. Kargar, Y. Barlas, M. M. Lacerda, J. X. Li, R. K. Lake, J. Shi, and A. A. Balandin, Appl. Phys. Lett. **111**, 252402 (2017).

[29] X. X. Li and J. L. Yang, J. Mater. Chem. C **2**, 7071 (2014).

[30] J. P. Perdew, K. Burke, and M. Ernzerhof, Phys. Rev. Lett. **78**, 1396 (1997).

[31] S. L. Dudarev, G. A. Botton, S. Y. Savrasov, C. J. Humphreys, and A. P. Sutton, Phys. Rev. B **57**, 1505 (1998).

[32] N. Sivadas, M. W. Daniels, R. H. Swendsen, S. Okamoto, and D. Xiao, Phys. Rev. B **91**, 235425 (2015).

[33] C. Song, W. Xiao, L. Li, Y. Lu, P. Jiang, C. Li, A. Chen, and Z. Zhong, Phys. Rev. B **99**, 214435 (2019).

[34] J. He, G. Ding, C. Zhong, S. Li, D. Li, and G. Zhang, J. Mater. Chem. C **7**, 5084 (2019).

[35] Z. L. Li, T. Cao, and S. G. Louie, J. Magn. Magn. Mater. **463**, 28 (2018).

[36] T. Holstein and H. Primakoff, Phys. Rev. **58**, 1098 (1940).

[37] See Supplemental Material at http://link.aps.org/supplemental/10.1103/PhysRevB.100.224427 for spin waves obtained by Holstein-Primakoff and Fourier transform, calculations of FM-AFM phase transition of ML, CGT, dynamics simulations of CGT ML, and SPC obtained with PBEsol functional.

[38] A. B. Sushkov, O. Tchernyshyov, W. Ratcliff, S. W. Cheong, and H. D. Drew, Phys. Rev. Lett. **94**, 137202 (2005).